Hexa-Active Vector Pulse Width Modulation in IPMSM Sensorless Drives Using Single DC-Link Current Sensor

Byung Ryang Park [1], Gyu Cheol Lim [1], Yongsu Han[2], and Jung-Ik Ha[1]
[1] Department of Electrical Engineering, Seoul National University, South Korea
[2] Department of Electronics Engineering, Myongji University, South Korea

***Abstract*—In cost-effective applications, the position sensorless drive using single current sensor (SD-SCS) is widely utilized due to the minimized number of sensors. However, the drive performance of the saliency-based SD-SCS is deteriorated due to the limited condition of phase current reconstruction (PCR) and the interference of voltage injection for both PCR and saliency-based position estimation. Therefore, this paper proposes an enhanced position estimation scheme based on the unified carrier-based injection. First, the error in injected voltage is reduced by using the unified carrier-based injection for PCR and saliency-based position estimation. Next, the motor parameter dependency in position estimation is eliminated by utilizing the phase current derivative measurements at each of the six active vectors. To verify the feasibility of the proposed method, the simulation and experimental results are presented about the enhanced drive performance of SD-SCS.**

***Index Terms*—Permanent magnet synchronous machine (PMSM), pulse-width modulation (PWM), sensorless drive, single current sensor (SCS).**

I. INTRODUCTION

The permanent magnet synchronous machine (PMSM) has been extensively used in various industries owing to its high power density and fast dynamics. For the field-oriented control of the PMSM, the phase currents and rotor position information are needed, which require the various sensors. However, in several industries such as home appliance, where cost, compactness, and reliability of the AC-drive system are important, minimizing the number of sensors is essential. As a result, the position sensorless drive utilizing a single current sensor is widely used in various industries [1]–[5].

When the single current sensor inverter is utilized, the phase current flows on the dc link path during active voltage vectors, as shown in Fig. 1. However, to achieve accurate reconstruction of the phase current, a minimum time duration of each active vector T_{min} is required due to several practical factors. The minimum duration T_{min} determined as (1), including the settling time T_{sett} for current oscillation caused by parasitic inductance, analog to digital conversion time T_{adc}, and dead time of the inverter T_{dead}.

$$T_{min} \geq T_{sett} + T_{adc} + T_{dead} \tag{1}$$

Since the T_{min} needs to be secured in each active vector, a current reconstruction dead zone (CRDZ) inevitably exists in the low-modulation and sector boundary regions, as shown in Fig. 2. To enable phase current reconstruction (PCR) within the CRDZ, several researches have been presented on modifying the pulse-width modulation (PWM) scheme [6]–[11]. As shown in Fig. 2, when the original voltage vector $V_{dqs}^{s^*}$ locates in the CRDZ, the measurement voltage vector $V_{dqs,m}^{s^*}$ is located in the first half period to enable PCR and the compensation voltage vector $V_{dqs,c}^{s^*}$ is calculated to maintain the average voltage reference. That is, the T_{min} is secured by the injected voltage for PCR within the CRDZ. Thanks to the previous efforts, the drive performance using the SCS is comparable to that of the three-phase current sensor system.

In addition to the SCS system, many studies have been performed on the position sensorless drive to further reduce the price and size of the AC drive system [12]–[19]. Especially, the inductance saliency of interior permanent magnet synchronous machine (IPMSM) is utilized to estimate the rotor position at the low-speed, where the magnitude of back electromotive force (EMF) is not

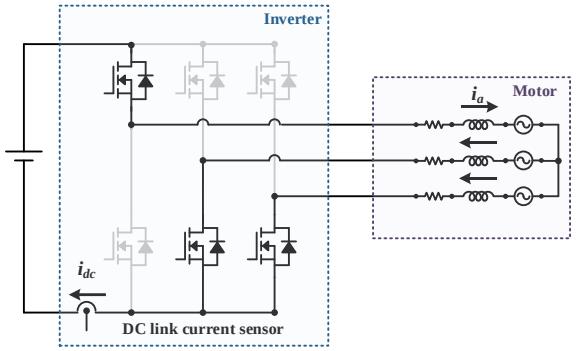

Fig. 1. Phase current reconstruction using single dc-link current sensor.

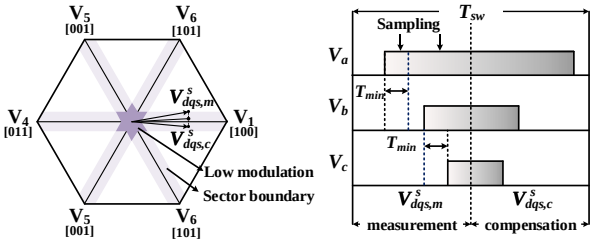

Fig. 2. Current reconstruction dead zone and current reconstruction methods in the dead zone.

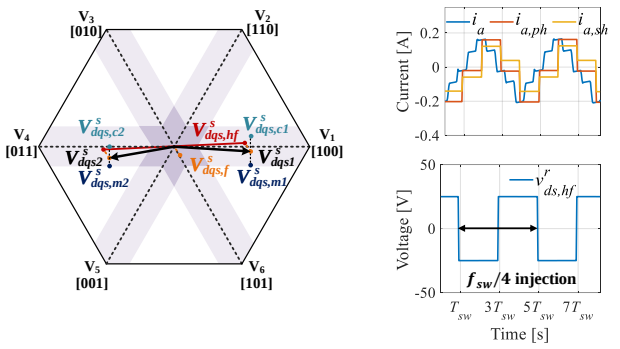

(a) (b)

Fig. 3. Saliency-based position sensorless drive. (a) Voltage vectors in the stationary referecne frame.(b) Phase current reconstruction.

TABLE I.
PHASE CURRENT RECONSTRUCTION ACCORDING TO VOLTAGE VECTORS

Voltage Vector	$\overrightarrow{V_{0,7}}$	$\overrightarrow{V_1}$	$\overrightarrow{V_2}$	$\overrightarrow{V_3}$	$\overrightarrow{V_4}$	$\overrightarrow{V_5}$	$\overrightarrow{V_6}$
DC-Link Current	Not available	i_a	$-i_c$	i_b	$-i_a$	i_c	$-i_b$

sufficiently large enough below a certain speed [12]–[14]. However, when the saliency-based sensorless drive is utilized in the SCS system, there is a limit to the position estimation accuracy due to errors in injected voltage and reconstructed high-frequency current.

Consequently, several methods have been introduced to improve saliency-based sensorless drive with single current sensor (SD-SCS) [1]–[5]. In [3], [4], the reconstruction error of high-frequency current is reduced by modifying the high-frequency voltage injection method or adjusting the current sampling timing within a PWM switching sequence. However, these methods are still affected by injected voltage errors for PCR and motor parameter errors. In [5], the machine drive performance of saliency-based SD-SCS is enhanced by removing the CRDZ in the low-modulation area and using the phase current derivatives for rotor position estimation. However, there still exists a parameter dependency for accurate rotor position estimation.

Therefore, this paper proposes an enhanced control shceme based on unified carrier-based injection for both PCR and saliency-based SD–SCS. The unified carrier-based injection secures the minimum duration T_{min} for both PCR and the saliency-based SD-SCS simultaneously, which enhances the overall machine drive performance. Furthermore, the parameter dependency in position estimation accuracy is eliminated based on the phase current derivative modeling at six active vectors.

II. SALIENCY-BASED SENSORLESS DRIVES USING SINGLE DC-LINK CURRENT SENSOR

When utilizing the single current sensor, the phase current is reconstructed from the dc-link current at each active vector, as shown in Table I. However, when the voltage vector locates in the CRDZ, where the minimum duration T_{min} is not secured, various methods have been presented to enable PCR. In this paper, the method in [8], which injects the minimum voltage within the CRDZ to ensure the T_{min}, is adopted for PCR.

TABLE II. PARAMETERS OF TARGET MOTOR

Symbol	Parameter	Nominal Value
PP	Pole Pair	4
V_{dc}	DC Link Voltage	200 V
$T_{e,rated}$	Rated Torque	4.77 Nm
$I_{s,rated}$	Rated Current	4.2 A
R_s	Stator Resistance	0.9 Ω
L_d / L_q	D / Q-axis Inductance	9.4 mH / 18.1 mH
λ_f	Flux Linkage	183 mV/(rad/s)

To further reduce the cost and size of AC drive system, the saliency-based sensorless drive is adopted in the low-speed region. Then, the high-frequency voltage is injected to track the inductance saliency, which includes the rotor position information. But, the additional voltage is also injected in CRDZ for PCR and this leads to an error in the high-frequency voltage for rotor position estimation. Furthermore, the limited current reconstruction condition using the SCS results an error in the high-frequency current. These error factors deteriorate the position estimation performance in the SCS system.

When the saliency-based sensorless drive is performed in the SCS system, the modified voltage references are shown in Fig. 3(a). The sum of the fundamental voltage vector $v^s_{dqs,f}$ and the high-frequency voltage $v^s_{dqs,hf}$ corresponds to the $v^s_{dqs,1}$. Since it locates in the CRDZ, the voltage vectors are generated with measurement voltage vector $v^s_{dqs,m1}$ and compensation voltage vector $v^s_{dqs,c1}$. Likewise, when the high-frequency voltage is injected in the opposite direction, the total voltage vector $v^s_{dqs,2}$ is generated with $v^s_{dqs,m2}$ and $v^s_{dqs,c2}$. As a result, the injected voltage for the saliency-based sensorless drive has an error due to the voltage injection for PCR in the CRDZ.

Also, to check the error factors in the saliency-based SD-SCS, the *d*-axis pulsating voltage injection method in [5] is utilized in the simulation. The parameters of the target motor are listed in Table II. Then, the operating condition corresponds to 50 r/min under no load, where the injection frequency is equal to a quarter of the switching frequency. As shown in Fig. 3(b), the reconstructed current $i_{a,sh}$ has an error with the current sensed with phase current sensor $i_{a,ph}$ due to the current sampling during the active vector. These error factors in the saliency-based SD-SCS deteriorate the position estimation accuracy.

III. PROPOSED SENSORLESS DRIVE USING CURRENT DERIVATIVES AT SIX ACTIVE VECTORS

In the previously presented PWM in [5], the phase current derivatives at V_1, V_3, and V_5 are used for the saliency-based SD-SCS. But, the motor parameter-based compensation is needed to accurately estimate the rotor position. In order to eliminate the parameter dependent

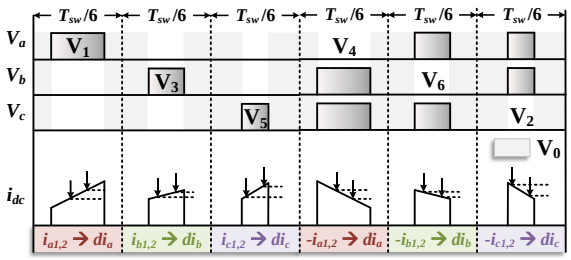

Fig. 4. Proposed PWM consisting of odd and even active vectors.

terms in phase current derivatives, this paper proposes the modified PWM, which utilizes the odd and even active vectors sequentially in a PWM period, as shown in Fig. 4

The duration of odd-active vectors $T_{x(x=1,3,5)}$ is determined, as represented in [5]. Also, each duration of even active vectors $T_{x(x=4,6,2)}$ is calculated from the switching period T_{sw}, the dc-link voltage V_{dc} and the d-q voltage reference $V_{dqs}^{s^*}$ in the stationary reference frame as

$$T_4 = -\frac{T_{sw}}{2V_{dc}} V_{ds}^{s^*} + \frac{T_{sw}}{6}$$

$$T_6 = \frac{T_{sw}}{4V_{dc}} V_{ds}^{s^*} - \frac{\sqrt{3}T_{sw}}{4V_{dc}} V_{qs}^{s^*} + \frac{T_{sw}}{6} \quad (2)$$

$$T_2 = \frac{T_{sw}}{4V_{dc}} V_{ds}^{s^*} + \frac{\sqrt{3}T_{sw}}{4V_{dc}} V_{qs}^{s^*} + \frac{T_{sw}}{6}.$$

To reduce PWM current ripple, the common duration of active vectors is replaced with zero vector duration T_0 as

$$T_0 = min(T_4, T_6, T_2). \quad (3)$$

Then, to eliminate the CRDZ in the low-modulation area, each active vectors includes the T_{min} and the duration of each active vector $T'_{x(x=4,6,2)}$ is finally determined as

$$\begin{aligned} T_4' &= T_4 - T_0 + T_{min} \\ T_6' &= T_6 - T_0 + T_{min} \\ T_2' &= T_2 - T_0 + T_{min}. \end{aligned} \quad (4)$$

In order to estimate the rotor position, the modeling of the phase current derivatives is needed at each of the even

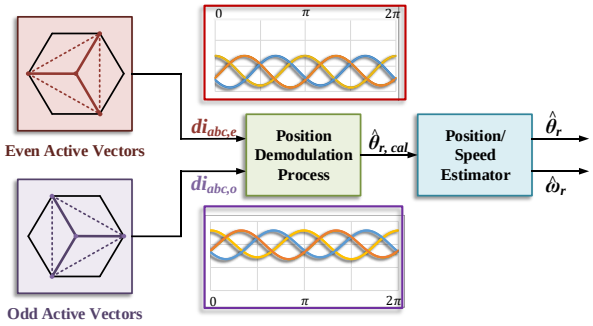

Fig. 5. Position demodulation scheme using phase current derivatives

active vectors. Among the three active vectors, the phase current derivative at the active vector of V_4 is representatively derived.

The phase voltage equation of IPMSM are written as

$$V_{xs} = R_s i_x + \frac{d\lambda_{xs}}{dt}, (x = a, b, c) \quad (5)$$

where V_{xs}, i_x, and λ_{xs} are stator voltage, current, and flux of phases a, b, and c.

At active vector of V_4 [011], the line-to-line voltage equations are derived as

$$V_{ab} = R_s\left(\frac{3}{2} i_{ds}^s - \frac{\sqrt{3}}{2} i_{qs}^s\right) + \frac{d}{dt}\left(\frac{3}{2}\lambda_{ds}^s - \frac{\sqrt{3}}{2}\lambda_{qs}^s\right) \quad (6)$$

$$V_{ac} = R_s\left(\frac{3}{2} i_{ds}^s + \frac{\sqrt{3}}{2} i_{qs}^s\right) + \frac{d}{dt}\left(\frac{3}{2}\lambda_{ds}^s + \frac{\sqrt{3}}{2}\lambda_{qs}^s\right) \quad (7)$$

Also, the d-q flux linkage λ_{dqs}^s in the stationary reference frame is represented as

$$\begin{bmatrix}\lambda_{ds}^s \\ \lambda_{qs}^s\end{bmatrix} = \begin{bmatrix}\sum L + \Delta L\cos 2\theta_r & \Delta L \sin 2\theta_r \\ \Delta L \sin 2\theta_r & \sum L - \Delta L \cos 2\theta_r\end{bmatrix}\begin{bmatrix}i_{ds}^s \\ i_{qs}^s\end{bmatrix} + \lambda_f \begin{bmatrix}\cos\theta_r \\ \sin\theta_r\end{bmatrix}, \quad (8)$$
$$\sum L = \frac{L_{ds} + L_{qs}}{2}, \Delta L = \frac{L_{ds} - L_{qs}}{2}.$$

From (6)-(8), the phase current derivative is derived and can be reconstructed from the dc-link current at the active vector of V_4. Likewise, the phase current derivatives of i_b and i_c are obtained as (9). Also, the phase current derivatives at odd active vectors are derived as (10).

$$\begin{aligned} \frac{di_{a,e}}{dt} &= \frac{-\frac{2V_{dc}}{3}(\sum L - \Delta L\cos 2\theta_r) + L_d(\omega_r\lambda_f + R_s i_{qs}^r)\sin\theta_r - L_q(L_d - L_q)\omega_r i_{qs}^r \cos\theta_r}{(\sum L)^2 - (\Delta L)^2} \\ \frac{di_{b,e}}{dt} &= \frac{-\frac{2V_{dc}}{3}\left(\sum L - \Delta L\cos\left(2\theta_r - \frac{2\pi}{3}\right)\right) + L_d(\omega_r\lambda_f + R_s i_{qs}^r)\sin(\theta_r - \frac{2\pi}{3}) - L_q(L_d - L_q)\omega_r i_{qs}^r\cos(\theta_r - \frac{2\pi}{3})}{(\sum L)^2 - (\Delta L)^2} \\ \frac{di_{c,e}}{dt} &= \frac{-\frac{2V_{dc}}{3}\left(\sum L - \Delta L\cos\left(2\theta_r - \frac{4\pi}{3}\right)\right) + L_d(\omega_r\lambda_f + R_s i_{qs}^r)\sin(\theta_r - \frac{4\pi}{3}) - L_q(L_d - L_q)\omega_r i_{qs}^r\cos(\theta_r - \frac{4\pi}{3})}{(\sum L)^2 - (\Delta L)^2} \end{aligned} \quad (9)$$

$$\begin{aligned} \frac{di_{a,o}}{dt} &= \frac{\frac{2V_{dc}}{3}(\sum L - \Delta L\cos 2\theta_r) + L_d(\omega_r\lambda_f + R_s i_{qs}^r)\sin\theta_r - L_q(L_d - L_q)\omega_r i_{qs}^r \cos\theta_r}{(\sum L)^2 - (\Delta L)^2} \\ \frac{di_{b,o}}{dt} &= \frac{\frac{2V_{dc}}{3}\left(\sum L - \Delta L\cos\left(2\theta_r - \frac{2\pi}{3}\right)\right) + L_d(\omega_r\lambda_f + R_s i_{qs}^r)\sin(\theta_r - \frac{2\pi}{3}) - L_q(L_d - L_q)\omega_r i_{qs}^r\cos(\theta_r - \frac{2\pi}{3})}{(\sum L)^2 - (\Delta L)^2} \\ \frac{di_{c,o}}{dt} &= \frac{\frac{2V_{dc}}{3}\left(\sum L - \Delta L\cos\left(2\theta_r - \frac{4\pi}{3}\right)\right) + L_d(\omega_r\lambda_f + R_s i_{qs}^r)\sin(\theta_r - \frac{4\pi}{3}) - L_q(L_d - L_q)\omega_r i_{qs}^r\cos(\theta_r - \frac{4\pi}{3})}{(\sum L)^2 - (\Delta L)^2} \end{aligned} \quad (10)$$

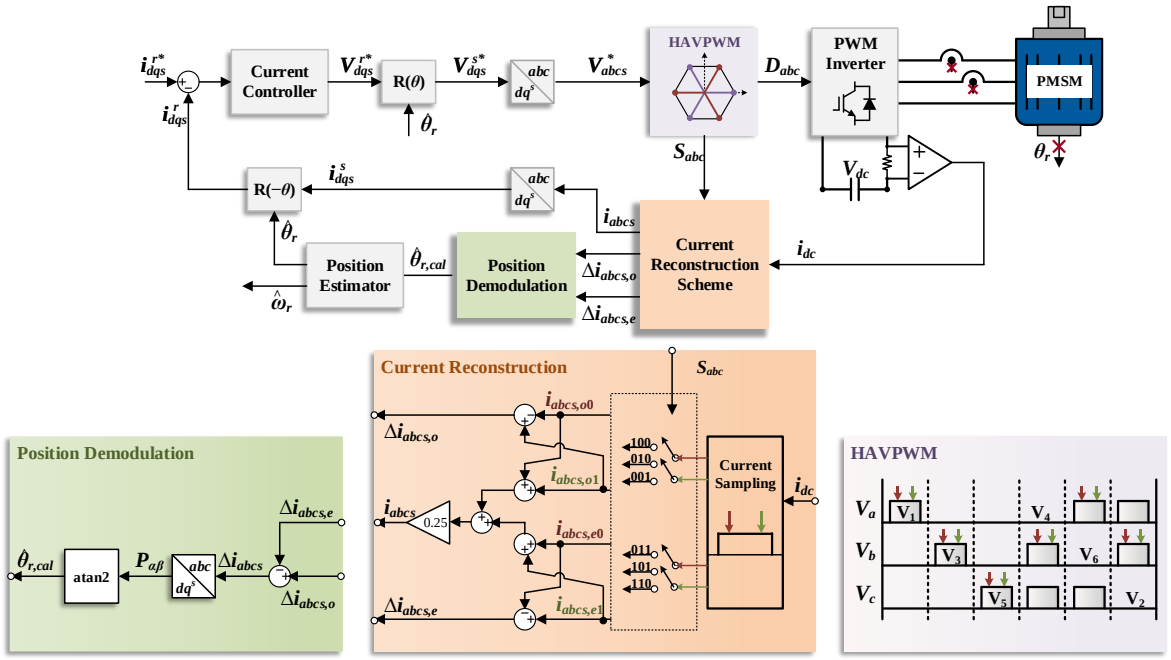

Fig. 6. Overall block diagram of proposed method.

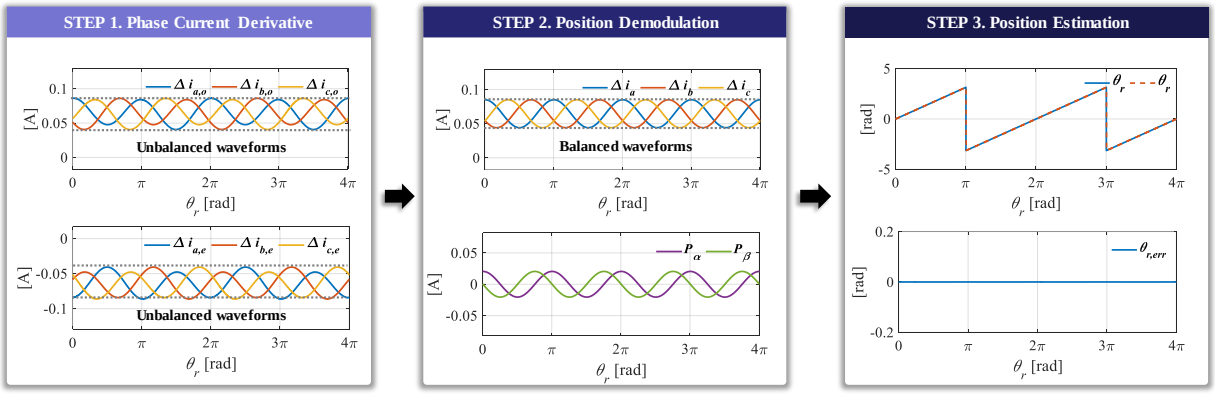

Fig. 7. Simulation result of proposed method at 100 r/min under rated load.

In order to eliminate the fundamental frequency terms in the phase current derivatives as (9)-(10), the current derivative measurements from both even and odd-active vectors are utilized and the current derivatives are finally determined as (11)-(12).

$$\frac{di_x}{dt} = \frac{\frac{di_{x,o}}{dt} - \frac{di_{x,e}}{dt}}{2} \quad (x = a, b, c) \tag{11}$$

$$\frac{di_a}{dt} = \frac{\frac{2V_{dc}}{3}(\sum L - \Delta L \cos 2\theta_r)}{(\sum L)^2 - (\Delta L)^2}$$

$$\frac{di_b}{dt} = \frac{\frac{2V_{dc}}{3}\left(\sum L - \Delta L \cos\left(2\theta_r - \frac{2\pi}{3}\right)\right)}{(\sum L)^2 - (\Delta L)^2} \tag{12}$$

$$\frac{di_c}{dt} = \frac{\frac{2V_{dc}}{3}\left(\sum L - \Delta L \cos\left(2\theta_r - \frac{4\pi}{3}\right)\right)}{(\sum L)^2 - (\Delta L)^2}$$

After position demodulation process as (13)-(14), the rotor position $\theta_{r,cal}$ is finally estimated from the demodulated signal P_α and P_β. As shown in Fig. 5, the rotor position is estimated from the phase current derivatives measurements at odd and even active vectors and position demodulation process.

$$P_\alpha = \frac{1}{3}\left(2\frac{di_a}{dt} - \frac{di_b}{dt} - \frac{di_c}{dt}\right) = \frac{-\frac{2V_{dc}}{3}\Delta L \cos 2\theta_r}{(\sum L)^2 - (\Delta L)^2}$$
$$P_\beta = \frac{1}{\sqrt{3}}\left(\frac{di_b}{dt} - \frac{di_c}{dt}\right) = \frac{\frac{2V_{dc}}{3}\Delta L \sin 2\theta_r}{(\sum L)^2 - (\Delta L)^2} \tag{13}$$

$$2\theta_{r,cal} = \text{atan2}(P_\beta, -P_\alpha) \tag{14}$$

The overall block diagram of proposed method consists of three parts: i) PWM scheme, ii) current reconstruction, and iii) position demodulation, as illustrated in Fig. 6. First, the hexa-active vector PWM (HAVPWM), which consists of odd and even active vectors sequentially, is utilized to obtain the current derivative measurements at six active vectors. Next, in the current reconstruction part, the dc-link current is sampled twice during each sixth switching state. In order to eliminate the parameter dependency in position

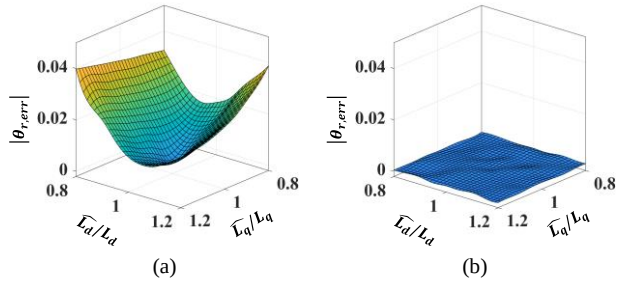

Fig. 8. Simulation results of the parameter dependency in position estimation at 100 r/min under rated load. (a) Conventional method. (b) Proposed method.

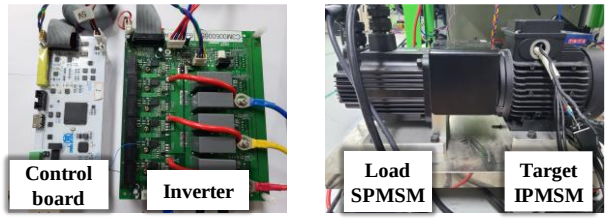

Fig. 9. Experimental setup.

estimation, phase current derivatives are obtained at each of the six active vectors. By subtracting the phase current derivatives from the odd and even active vectors, the parameter dependent terms in the phase current derivatives are eliminated. Finally, using the position demodulation process as (13)-(14) and the position estimator in [18], the rotor position and motor speed are estimated.

To validate the position estimation performance of the proposed method, the simulation is performed at 100 r/min under rated load condition. As shown in Fig. 7, the current derivatives obtained from the odd and even active vectors have unbalanced waveforms due to the fundamental frequency terms as (9)-(10). However, by utilizing the difference between the current derivatives obtained from odd and even active vectors, the phase current derivatives have balanced waveforms, which contains only second order harmonics as (12). Consequently, the rotor position is accurately estimated without the motor parameter–based compensation for the fundamental frequency terms

Additionally, the simulation is performed to compare the position estimation accuracy with the conventional method under the motor parameter variation. When the *d-q* inductance L_d, L_q vary from 80% to 120% of their nominal values, the position estimation accuracy is shown in Fig. 8. With the conventional method, the position estimation error exists with parameter errors, as shown in Fig. 8(a). However, when the proposed method is utilized, the position estimation error is almost zero regardless of the parameter accuracy, as shown in Fig. 8(b).

IV. Experimental Results

To verify the feasibility of the proposed method, various experiments are conducted. The photographs of the experimental setup are shown in Fig. 9. The parameters of the target IPMSM are the same as the simulation. The bandwidths of the speed controller and current controller

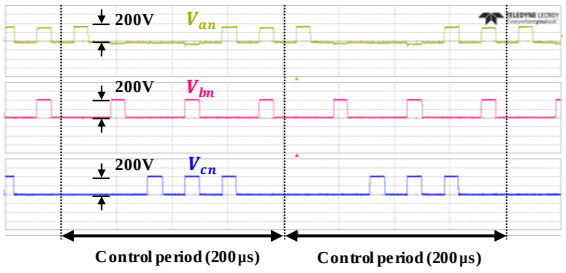

Fig. 10. Pole voltage waveforms of the proposed PWM scheme.

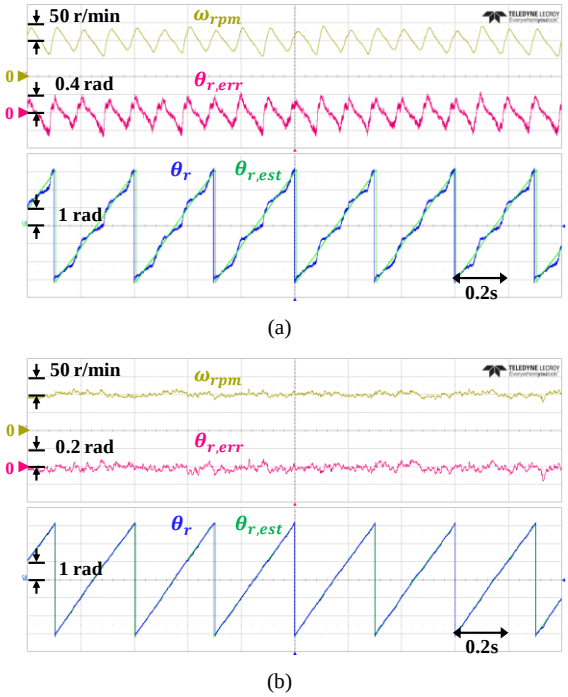

Fig. 11. Position estimation results at 100 r/min under no load. Estimation methods: (a) Conventional method. (b) Proposed method.

are set to 10 Hz and 150 Hz, respectively, and the switching frequency f_{sw} is set to 5 kHz. Then, the minimum duration of each active vector $T_{min,s2}$ is set to 13 μs for the double current sampling. Also, the shunt resistor of 10 mΩ is located in the negative rail of the dc-link, and the incremental encoder with 4096 PPR is utilized to monitor the rotor position. And the proposed method, including the position estimation algorithm and PWM scheme, are implemented on the TMS320F28379s.

Fig. 10 shows the pole voltage waveforms when the proposed HAVPWM is utilized. The odd and even active vectors are generated sequentially including the minimum time $T_{min,s2}$.

Fig. 11 shows the position estimation performance at 100 r/min under no load. The conventional method in Fig. 11(a) corresponds to the high-frequency injection method with SVPWM in [1]. The position estimation accuracy of the proposed method is smaller than that of the conventional method, as shown in Fig. 11(b).

Fig. 12 shows the position estimation performance at 100 r/min under rated load. The conventional method has

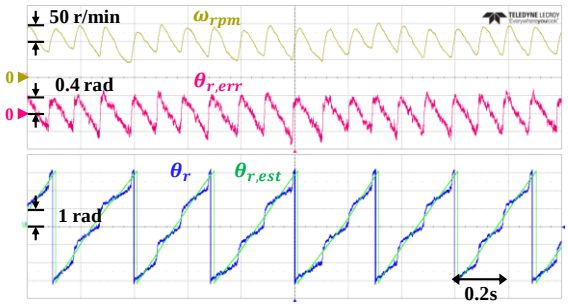

(a)

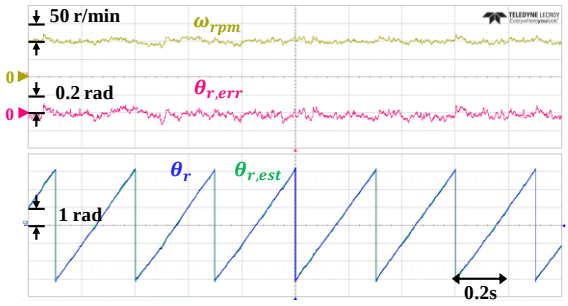

(b)

Fig. 12. Position estimation results at 100 r/min under rated load. Estimation methods: (a) Conventional method. (b) Proposed method.

shown the deteriorated position estimation accuracy at rated load. However, the position estimation accuracy is almost same with the proposed method, regardless of the operating condition.

Fig. 13 shows the dynamic response when the step speed control is performed from 50 r/min to -50 r/min and vice versa. The position estimation error remains within 0.08 rad.

Fig. 14 shows the dynamic response when the step load is applied under zero speed control. The rotor position is well estimated even when the step load is abruptly applied.

V. Conclusion

This paper proposes the PWM scheme, consisting of the hexa-active vectors in the switching period, to enhance the drive performance of saliency-based sensorless drive with single current sensor (SD-SCS). Based on the phase current derivative modeling at each of six active vectors, the parameter independent position estimation method is proposed. Also, the unified carrier-based injection for both current reconstruction and position estimation improves the position estimation accuracy. The experimental results verify the enhanced drive performance of SD-SCS with the proposed method. Furthermore, the position estimation accuracy is ensured regardless of the load condition owing to the elimination of parameter dependency in position estimation scheme.

Acknowledgment

This work was supported in part by the Korea Institute of Energy Technology Evaluation and Planning (KETEP) grant funded by the Korea government the Ministry of Trade, Industry, and Energy of the Republic of Korea (MOTIE) (20212020800020), and in part by the BK21 FOUR program of the Education and Research Program for Future ICT Pioneers, Seoul National University in 2023.

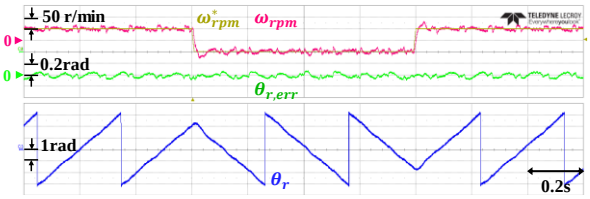

Fig. 13. Step speed response from 50 r/min to -50 r/min under no load.

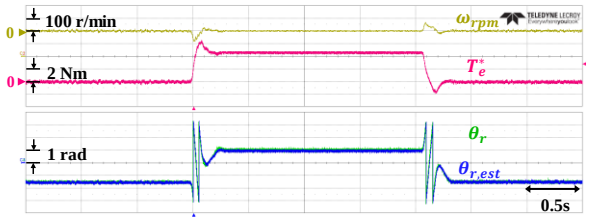

Fig. 14. Step load response under zero speed control.

References

[1] S.-C. Yang, "Saliency-Based Position Estimation of Permanent-Magnet Synchronous Machines Using Square-Wave Voltage Injection With a Single Current Sensor," IEEE Transactions on Industry Applications, vol. 51, no. 2, pp. 1561–1571, Mar. 2015, doi: 10.1109/TIA.2014.2358796.

[2] B. R. Park, G. C. Lim, Y. Han, J. Lee, and J.-I. Ha, "Saliency-Based Sensorless IPMSM Drives Using Derivatives of Phase Currents With Single DC-Link Current Sensor," in 2023 IEEE Applied Power Electronics Conference and Exposition (APEC), Mar. 2023, pp. 1402–1408. doi: 10.1109/APEC43580.2023.10131390.

[3] J.-H. Im and R.-Y. Kim, "Improved Saliency-Based Position Sensorless Control of Interior Permanent-Magnet Synchronous Machines With Single DC-Link Current Sensor Using Current Prediction Method," IEEE Transactions on Industrial Electronics, vol. 65, no. 7, pp. 5335–5343, Jul. 2018, doi: 10.1109/TIE.2017.2777382.

[4] L. Tian, Z. Wang, Q. Yu, C. Tang, and H. Zhang, "Current Reconstruction by One-Step Compensation for Permanent Magnet Synchronous Motor With Fixed Sampling Interval in Position Sensorless Control," IEEE Transactions on Industrial Electronics, vol. 70, no. 1, pp. 200–210, Jan. 2023, doi: 10.1109/TIE.2022.3156155.

[5] B. R. Park, G. C. Lim, Y. Han, and J.-I. Ha, "Saliency-Based Sensorless Control Using Current Derivative in IPMSM Drives With Single DC-Link Current Sensor," IEEE Transactions on Industrial Electronics, pp. 1–10, 2023, doi: 10.1109/TIE.2023.3274858.

[6] F. Blaabjerg, J. K. Pedersen, U. Jaeger, and P. Thoegersen, "Single current sensor technique in the DC link of three-phase PWM-VS inverters: a review and a novel solution," IEEE Transactions on Industry Applications, vol. 33, no. 5, pp. 1241–1253, Sep. 1997, doi: 10.1109/28.633802.

[7] H. Kim and T. M. Jahns, "Phase Current Reconstruction for AC Motor Drives Using a DC Link Single Current Sensor and Measurement Voltage Vectors," IEEE Transactions on

Power Electronics, vol. 21, no. 5, pp. 1413–1419, Sep. 2006, doi: 10.1109/TPEL.2006.880262.
[8] J.-I. Ha, “Voltage Injection Method for Three-Phase Current Reconstruction in PWM Inverters Using a Single Sensor,” IEEE Transactions on Power Electronics, vol. 24, no. 3, pp. 767–775, Mar. 2009, doi: 10.1109/TPEL.2008.2009451.
[9] J.-I. Ha, “Current Prediction in Vector-Controlled PWM Inverters Using Single DC-Link Current Sensor,” IEEE Transactions on Industrial Electronics, vol. 57, no. 2, pp. 716–726, Feb. 2010, doi: 10.1109/TIE.2009.2028361.
[10] J. Lu, X. Zhang, Y. Hu, J. Liu, C. Gan, and Z. Wang, “Independent Phase Current Reconstruction Strategy for IPMSM Sensorless Control Without Using Null Switching States,” IEEE Transactions on Industrial Electronics, vol. 65, no. 6, pp. 4492–4502, Jun. 2018, doi: 10.1109/TIE.2017.2767542.
[11] H. Choi, J.-I. Ha, and K. Lee, “Ultra-Low Inductance PMSM Drive Using a DC Current Sensor,” IEEE Transactions on Industrial Electronics, pp. 1–10, 2023, doi: 10.1109/TIE.2023.3288203.
[12] S. Morimoto, K. Kawamoto, M. Sanada, and Y. Takeda, “Sensorless control strategy for salient-pole PMSM based on extended EMF in rotating reference frame,” IEEE Transactions on Industry Applications, vol. 38, no. 4, pp. 1054–1061, Jul. 2002, doi: 10.1109/TIA.2002.800777.
[13] G. Wang, M. Valla, and J. Solsona, “Position Sensorless Permanent Magnet Synchronous Machine Drives—A Review,” IEEE Transactions on Industrial Electronics, vol. 67, no. 7, pp. 5830–5842, Jul. 2020, doi: 10.1109/TIE.2019.2955409.
[14] J. Shim, B. R. Park, S. Choi, and J.-I. Ha, “Learning-based Position Sensorless Control in Low-speed Region for SMPMSM,” in 2022 IEEE Energy Conversion Congress and Exposition (ECCE), Oct. 2022, pp. 1–5. doi: 10.1109/ECCE50734.2022.9947561.
[15] J.-I. Ha and S.-K. Sul, “Sensorless field-orientation control of an induction machine by high-frequency signal injection,” IEEE Transactions on Industry Applications, vol. 35, no. 1, pp. 45–51, Jan. 1999, doi: 10.1109/28.740844.
[16] J.-H. Jang, S.-K. Sul, J.-I. Ha, K. Ide, and M. Sawamura, “Sensorless drive of surface-mounted permanent-magnet motor by high-frequency signal injection based on magnetic saliency,” IEEE Transactions on Industry Applications, vol. 39, no. 4, pp. 1031–1039, Jul. 2003, doi: 10.1109/TIA.2003.813734.
[17] S. Kim, J.-I. Ha, and S.-K. Sul, “PWM Switching Frequency Signal Injection Sensorless Method in IPMSM,” IEEE Transactions on Industry Applications, vol. 48, no. 5, pp. 1576–1587, Sep. 2012, doi: 10.1109/TIA.2012.2210175.
[18] Y.-D. Yoon, S.-K. Sul, S. Morimoto, and K. Ide, “High-Bandwidth Sensorless Algorithm for AC Machines Based on Square-Wave-Type Voltage Injection,” IEEE Transactions on Industry Applications, vol. 47, no. 3, pp. 1361–1370, May 2011, doi: 10.1109/TIA.2011.2126552.
[19] J. Lee, B. R. Park, G. C. Lim, and J.-I. Ha, “Hybrid Pulse Width Modulation with Current Derivative Measurement for PMSM Sensorless Control,” in 2023 IEEE Applied Power Electronics Conference and Exposition (APEC), Mar. 2023, pp. 1090–1096. doi: 10.1109/APEC43580.2023.10131520.